Cation exchange inducing properties of defect variant perovskite A_2BX_6: Substituting Sn^{+4} with Te^{+4}

Muhammad Faizan[1,2*], Jiahao Xie [2], Shah Haidar Khan[1] Ghulam Murtaza[3]

[1]Department of Physics, University of Peshawar, Peshawar 25120, Pakistan

[2]State Key Laboratory of Superhard Materials and School of Materials Science and Engineering, Jilin University, Changchun 130012, China

[3]Materials Modeling Lab, Department of Physics, Islamia College University, Peshawar 25120, Pakistan

*Correspondence: faizanstd@uop.edu.pk

Abstract: Metal halide perovskites have attracted significant research attention over the last few years primarily in the context of solar cell technology. However, the toxic lead in these materials has raised potential environmental concerns. We designed and explored lead free defect perovskite based on mixed tin and tellurium, $Rb_2Sn_{1-x}Te_xI_6$ ($0 \leq x \leq 1$), based on density functional theory. The lattice constant, optimized volume, bond length, tolerance factor, and formation energies are calculated for $x = 0.0, 0.25, 0.50, 0.75$, and 1. The lattice parameter as well as the optimized volume increase linearly as a function of the Te contents in $Rb_2Sn_{1-x}Te_xI_6$. The calculated band structure indicates semiconducting nature with increasing band gap as a function of the Te proportion. Optical properties such as the dielectric function, absorption coefficient, effective masses, exciton binding energies, and spectroscopic-limited-maximum-efficiency are also simulated. The calculated dielectric spectra are found similar to other semiconductors and their absorption spectra are mostly concentrated in the visible energy range. The effective masses of the charge carriers are derived from the HSE06 band structures and used, together with the dielectric constant, for finding the exciton binding energies. We found that the $Rb_2Sn_{1-x}Te_xI_6$ Perovskites exhibit several desirable properties, including substantial stability, suitable band gap, and remarkable optical absorption. In particular, $Rb_2Sn_{0.75}Te_{0.25}I_6$ and $Rb_2Sn_{0.50}Te_{0.50}I_6$ have favorable direct band gaps of 1.35 eV and 1.44 eV for single-junction photovoltaic applications. Our work provides key directions by which one can efficiently find the best doping atoms and optimal doping level to enhance the optoelectronic performance of A_2BX_6.

1. Introduction

During the last decade, significant progress has been observed in the field of halide perovskites (HPs) due to its promising role in the future photovoltaic technology.[1-4] The power conversion efficiency (PCE) of the solar cells based on HPs has improved considerably, reaching 25%[5] in a few years. The PCE achieved so far is comparable to the commercially available materials such as silicon (c-Si@27.6%) and copper indium gallium selenide (CIGS@23.4%).[5-6] Such a rapid increase in the PCE of lead based perovskite is mainly due to a suitable band gap, high optical absorption, ambipolar nature of charge transport, and long-photo-generated carrier diffusion lengths.[2, 7-9] However, despite all the progress achieved, the organic-inorganic halide perovskites (OIH-PVKs) have some serious issues: most notably the toxic nature of lead (Pb) and instability against moisture, high temperature, and light.[7, 10-11] The presence of the toxic Pb in high performance OIH-PVKs causes environmental contamination and some brain related symptoms such as intellectual disability.[10, 12] Similarly, the highly efficient OIH-PVKs contain organic cations on A-site, such as formamidinium ($CH(NH_2)_2$) or methylammonium (CH_3NH_3), which are highly volatile and hygroscopic.[13] This makes OIH-PVKs highly instable and tends to degrade rapidly in humid environment. Thus both the issues undoubtedly hinder further development of perovskite photovoltaic technology, opening diverse opportunities for researchers to replace Pb in hybrid halide perovskites with other nontoxic benign metals.[14-15] Concerted efforts have led to the development of nontoxic and air-stable halide perovskite with the hope that the problems mentioned above may be overcome whilst key properties are preserved for the emerging perovskite solar cells.[16-24]

There are two possible ways for making the perovskite related absorbers suitable for effective commercialization. The first strategy is to replace both the organic (monovalent) and Pb (divalent) cations in $AB^{2+}X_3$ perovskite with other suitable elements. The most obvious choice for the A-site cation is Cs^+ and Rb^+ whereas, for B^{2+}, some non-toxic divalent cations from group 2, group 12, and group 14 (Sn^{2+} and Ge^{2+}) may be considered. This in turn can significantly enhance perovskite thermal/moisture stability. Among these, only the Sn-based halide perovskite have achieved reasonable PCEs of magnitude 6.4%.[18] The second route is to design alternative all-inorganic perovskites by introducing trivalent (Bi^{3+} and Sb^{3+}), tetravalent (Sn^{4+} and Te^{4+}) and multivalent (Ag^+ and Bi^{3+}) cations in $AB^{2+}X_3$ structure.[25] This results in Pb-free perovskite derivatives of the

type $A_3B_2^{3+}X_9$, $A_2B^{4+}X_6$, and $A_2B^+B^{3+}X_6$ (A= Cs or monovalent inorganic ion, B= non-Pb trivalent/tetravalent cation, and X= halogen).[26] Trivalent and tetravalent substitution transforms the 3-dimensional (3D) and octahedral corner-sharing $AB^{2+}X_3$ perovskite into 2D and 0D perovskite with the corresponding octahedral edge-sharing and face-sharing environment. The multivalent substitution retains the same 3D structure wherein every pair of B-cations in $AB^{2+}X_3$ is replaced by one B^+ (Cu^+/Ag^+) and one B^{3+} (Bi^{3+}/In^{3+}) cation.[25] Many halide perovskites (HPs) have been theoretically designed and experimentally synthesized based on the multi and/or trivalent substitution, such as Cu^+, Ag^+, Bi^{3+}, and Sb^{3+} (e.g. $Cs_3Bi_2I_9$ 2.2 eV, $Cs_3Sb_2I_9$ 2.4 eV, and $Cs_2AgBiBr_6$ 2.2 eV).[21, 27-28] Such HPs have shown promising photovoltaic properties, including better stability against moisture and excess carrier recombination lifetime. However, their suboptimal band gap is undesirable, making them unsuitable for photovoltaic applications.[29]

Recently, the A_2BX_6 perovskite have attracted increasing attention for use in photovoltaic technology and as an alternative to OIH-PVKs due to the non-/or less-toxic nature. In comparison to ABX_3, the A_2BX_6 structure exhibits enhanced air and moisture stability under ambient conditions, correlating with the presence of tetravalent B-cation (formally 4+ oxidation in A_2BX_6 compared with 2+ in ABX_3).[23, 30-31] The structure contain ordered vacancies with isolated $[BX_6]^{2-}$ octahedra formed by the ordered removal of half of the B-site cation from the fully occupied ABX_3 structure, more recently referred to as vacancy ordered double perovskite or defect perovskite.[22, 31] Unlike the ideal perovskite, the $[BX_6]^{2-}$ octahedra in A_2BX_6 structure do not share vertices, and can be described as zero-dimensional perovskites.[32]

Various efforts have been made to develop defect perovskites A_2BX_6. Among them, the Sn-based materials are of great interest and demonstrated the best PCE (~8.5%).[19] Initial study on such HPs was performed by Lee et al, reporting Cs_2SnI_6 as a hole transport material in dye-sensitized solar cells (DSSCs).[30] The compound adopts cubic $Fm\bar{3}m$ type structure at ambient temperature, show enhance air/moisture stability, n-type electrical conductivity, direct band gap (~1.3 eV) and visible light absorption, all of which are favorable for most of the photovoltaic applications.[22-23, 30] Replacing 'Cs' with the smaller 'Rb' cation produce Rb_2SnI_6, accompanied by major changes in crystal structure and the subsequent optoelectronic properties.[33] Rb_2SnI_6 crystallize in three different phases (Cubic, Tetragonal, and Monoclinic)[33-34] and like Cs_2SnI_6, exhibit n-type electrical conductivity. Similarly, several Sn-based representatives of the A_2BX_6 family were also reported, for instance, K_2SnX_6 (X= Cl, Br, I)[35], $Cs_2Sn(I,Br)_6$[36], and Cs_2SnX_6 (X = Cl, Br, I).[31, 37] During the

past few years, research on A_2BX_6 based perovskites expanded to include other tetravalent cations, most notably, Ti(IV)[13, 29], Te(IV)[22], Ge(IV)[38], Pd(IV)[39-40], and Pt(IV)[41-42], thus paving the way to replace Sn in A_2SnX_6. In this context, Ju and his co-workers[13, 29] studied a series of Ti-based perovskites with general composition A_2TiX_6 (A = K, Rb, Cs, In, MA (methylammonium), FA (formamidinium) ; X = I, Br, or Cl). The compounds, namely K_2TiI_6, Rb_2TiI_6, Cs_2TiI_6, and In_2TiI_6 possess optimum band gap (1.0−1.8 eV) and desired electronic/optical properties as visible-light absorber materials for PV applications. Maughan et al.[22] carried out an integrated study by combining theory and experiment to understand the structure-property relationship in $Cs_{2(}Sn/Te)I_6$ defect perovskite. The study also reported the electronic, optical, and defect properties of Sn and Te doped solid solution, $Cs_2Sn_{1-x}Te_xI_6$. Ma and Li[38] incorporated Ge in Cs_2SnI_6, to see the effect on the structure as well electronic, elastic, and thermodynamic nature of $Cs_2Sn_{1-x}Ge_xI_6$. Similarly, palladium (Pd) based A_2BX_6 perovskites have been reported in many studies for a wide array of optoelectronic applications.[39, 42-44] In a recent study, Schwartz synthesized Cs_2PtI_6 using solution processing techniques.[41] The study reported a band gap of 1.4 eV and high optical absorption $> 10^5$ cm^{-1}, suggesting Cs_2PtI_6 as a possible layer in single- or multi-layer photovoltaic devices.

In extension, doping has been considered as an effective strategy to improve the stability and the fundamental properties of optoelectronic semiconductors.[45] Doping engineering relies on the incorporation of small amount of impurities into the host, causing change in the stability and photovoltaic performance of halide perovskites.[46] It has been successfully applied in low dimensional as well as other perovskites to understand the crystal symmetry and band gap engineering.[47-48] Previously, several groups reported impurity doping in halide perovskite. For example, Zhou et al.[49] fabricated Bi-doped organometal halide perovskite and found ultrabroad photoluminescence and electroluminescence. They further suggest low cost and earth-abundant perovskite semiconductors for different optical sources. The same authors also examined the effect of various metal doping in lead halide perovskite.[46] In particular, the metallic elements, such as Bi, Rb, Sr, and Mn, were incorporated as dopants for improving the performance of halide perovskites. Another group of researchers tuned the efficiency of Sn-based perovskite solar cells (PSCs) with mixed A-site organic cations. The author's reported a PCE of magnitude 8.12% for $(FA)_{0.75}(MA)_{0.25}SnI_3$.[50] Similarly, in A_2BX_6 perovskite, successful doping have been reported, for instance, Tan and his co-workers[12] prepared the Bi-doped Cs_2SnI_6 and confirmed blue emission at

455 nm and an outstanding photoluminescence quantum yield (PLQY). The reported PLQY is up to 80% which is the highest ever reported value among all inorganic Pb-free perovskites. Yuan et al.[51] reported the thermal stability and optical properties of $Cs_2SnI_{6-x}Br_x$ (x= 0-6) for potential applications in solar cells.

Herein, for the first time, we report a series of lead-free A_2BX_6 mixed tin and tellurium perovskites using element mixing strategy. We chose Rb_2SnI_6 as a host and Te as the dopant for a Pb-free, and stable perovskite $Rb_2Sn_{1-x}Te_xI_6$ ($0 \leq x \leq 1$). The successful substitution of Sn by Te is due to the close match between the ionic radii of Sn and of Te. We systematically assess the geometric structures, electronic, and optical properties of the selected perovskite derivatives using the rules of density functional theory in order to find better candidates for optoelectronics and solar cells application. The $Rb_2Sn_{1-x}Te_xI_6$ compounds adopt cubic $Fm\overline{3}m$ structure across the entire range of Te substitution. The compositional influence on the electronic structure and optical properties are then studied using the highly successful modified Becke Johnson and Heyd-Scuseria- Ernzerhof functionals. The band gap of $Rb_2Sn_{1-x}Te_xI_6$ alloyed compounds increase linearly with the increasing Te content, leading to a tunable range of 0.86 to 2.18 eV. Our results on the optical properties show that the Te-doped material exhibits significant absorption in the visible range, suggesting these materials as promising solar light harvesters. The suitable band gap, enhance stability, and high optical absorption make them ideal candidates for a wide range of applications, from single-junction devices and top/bottom cells for tandem photovoltaic to light-emitting devices.

2. First Principles Calculations

First-principles calculations were performed using the Vienna *ab initio* Simulation Package (VASP), based on DFT.[52] The standard projector augmented wave (PAW) method was adopted to describe the ion-electron interactions.[53] A plane-wave cutoff energy of 450 eV was employed in all the calculations, so as to avoid the error arising due to the Pulay stress.[54] The $4s^2 4p^6 5s^1$ (Rb), $4d^{10}5s^25p^2$ (Sn), $4d^{10}5s^25p^4$ (Te) and $5s^25p^5$ (I) electrons were treated explicitly as valence electrons. Electronic structure calculations were performed for the 9-atoms unit cell of Rb_2SnI_6 with 0%, 25%, 50%, 75%, and 100% Te concentrations replacing Sn. Each structure was geometrically relaxed using the Perdew–Burke–Ernzerhof (PBE) exchange–correlation (XC) functional.[55] For the electronic structure calculations, we used the most accurate scheme of

modified Becke Johnson (mBJ)[56] and Heyd-Scuseria- Ernzerhof (HSE)[57] functionals. The HSE06 functional incorporates 75% exchange and 100% of the correlation energies from PBE together with the exact exchange (α) contribution of 25%. K-point sampling for the Brillouin zone was done with Monkhorst–Pack scheme[58] centered at Γ with a grid spacings of $0.02 \times 2\pi$ Å^{-1} both for ionic and self-consistent field (SCF) iterations. The convergence criteria for the forces (in ionic step iterations) and energy (in SCF iterations) were selected as 10^{-2} eV Å^{-1} and 1.0×10^{-5} eV, respectively, whereas 8000 bands were chosen for band gap calculations. Compositions corresponding to 25, 50, 75, and 100% Te concentration were generated using the Material Studio package and all the schematic representation of the crystal structures were rendered by the VESTA plotting tool.[59] Full details of the optic calculation including dielectric function, absorption coefficient, and exciton binding energy are given in the Supporting Information (SI).

3. Results and Discussion

3.1. Geometrical Properties

The $Rb_2Sn_{1-x}Te_xI_6$ ($0 \leq x \leq 1$) alloyed compounds crystallize in face-centered cubic structure with space group $Fm\bar{3}m$ (No. 225). The Rb atoms occupy 8c site, B-atoms (Sn/Te) occupy 4a site, and iodide anion reside at the 24e Wyckoff site. The optimized geometries of $Rb_2Sn_{1-x}Te_xI_6$ are depicted in Figure 1. The structure can be derived from the corresponding ABX$_3$ perovskite by removing half of the B-atoms at the octahedral cluster.[7] The cage between [BI$_6$] octahedra is filled with A-cations which is surrounded by twelve I-anions. Each B-cation coordinates with six iodide ions (with 2 I-atoms in the apical and 4 in the equatorial direction). Here the [BI$_6$] framework can be seen to be isolated, compared with the corner sharing arrangement of the ABX$_3$ perovskite. Due to such structural change, the B-X bond length falls shorter in A$_2$BX$_6$, correlating with the high chemical stability. The lattice parameters obtained at PBE level and the available experimental data on $Rb_2Sn_{1-x}Te_xI_6$ are presented in Table 1. To our knowledge, only the end members (Rb_2SnI_6 and Rb_2TeI_6) were synthesized experimentally.[34, 60] Our calculations reveal lattice constants of magnitude 11.87 Å for Rb_2SnI_6 and 11.92 Å for Rb_2TeI_6, with a small deviation of ~2% from experimentally reported values. For mixed Sn-Te compounds, a slight increase in the lattice constant was observed in accordance with Te contribution (Figure S1). Due to the lack of experimental data, the lattice constant for the compounds with composition $x = 0.25$, 0.50, and 0.75 were not provided, we hope that our calculated data can act as a reference for future studies.

For doped systems, we have noticed that the optimized lattice parameters are the same for the face-centered as well as the apex position i.e. doping site does not affect the cell parameters. Therefore, we only considered face-centered doping in this study. Further, we see that the unit cell volume is increased with the increasing Te concentration (Figure S1). The increase in volume is mainly caused by the replacement of Sn^{4+} with Te^{4+} during the substitution. To better understand the geometric structures, we calculated different bond lengths after geometry optimization and presented them in Table S1 along with available experimental results. The obtained results show significant discrepancy between short and long bond lengths. The bond lengths Rb-B and B-I (B = Sn/Te) lie in the range of 5.13–5.16 Å and 2.90–2.96 Å, respectively. The increase in bond lengths of Rb-B and B-I may be attributed to the difference in electronegativity values of Sn and Te.
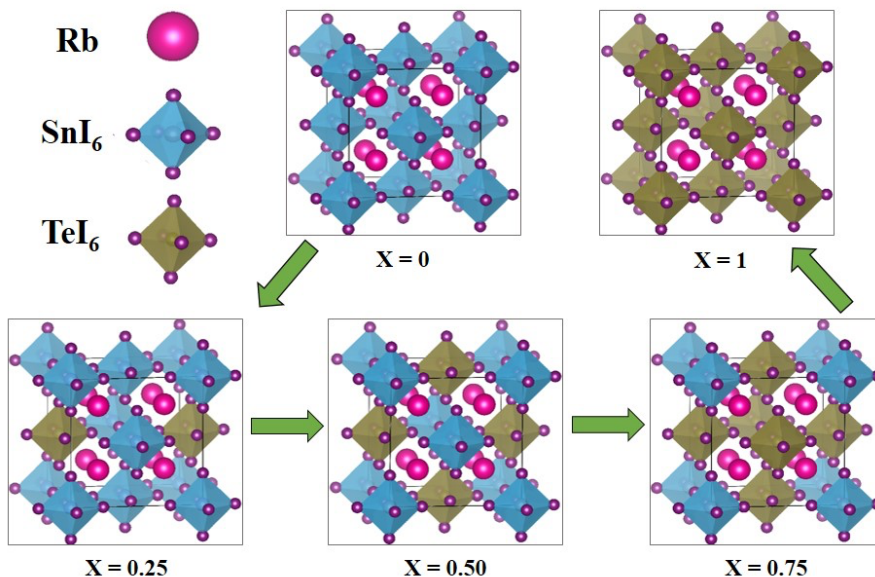

Figure 1. The optimized crystal geometries of $Rb_2Sn_{1-x}Te_xI_6$ ($0 \leq x \leq 1$) perovskites. Rb is in Pink, SnI_6 and TeI_6 octahedra are shaded in light blue and brown, respectively.
The crystal ionic radius of I^{-1} is 206 pm and that of Rb is 166 pm. Sn has 83^{+4} and Te^{+4} 111 pm. Is the figure drawn to scale? (Ref: https://en.wikipedia.org/wiki/Ionic_radius; Acta Cryst. (1976). A32, 751-767
https://doi.org/10.1107/S0567739476001551)

Table 1. Calculated lattice parameters for the $Rb_2Sn_{1-x}Te_xI_6$ ($0 \leq x \leq 1$) perovskites at the PBE-GGA level. The experimental lattice constants are listed in parallel.

	Lattice constants (Å)	Angles(°)

	a	b	c	Exp.	α	β	γ
0% Te (Rb$_2$SnI$_6$)	11.87	11.87	11.87	11.62[34]	90	90	90
25% Te (Rb$_2$Sn$_{0.75}$Te$_{0.25}$I$_6$)	11.88	11.88	11.88	----	90	90	90
50% Te (Rb$_2$Sn$_{0.50}$Te$_{0.50}$I$_6$)	11.89	11.89	11.87	----	90	90	90
75% Te (Rb$_2$Sn$_{0.25}$Te$_{0.75}$I$_6$)	11.90	11.90	11.90	----	90	90	90
100% Te (Rb$_2$TeI$_6$)	11.92	11.92	11.92	11.67[60]	90	90	90

In order to get a qualitative description of the crystallographic stabilities and structural distortion, we use a widely used geometric parameter, the tolerance factor (t), introduced by V. M. Goldschmidt.[61] The t factor can be used extensively to predict the formation of a stable perovskite material by using the following expression:

$$t = \frac{(r_A + r_X)}{\sqrt{2}(r_B + r_X)}$$

(where r_A, r_B, and r_X are the radii of A, B, and X site atoms). For an ideal cubic perovskite structure, t should be close to 1. Similarly, another factor responsible for the formability of perovskite materials is the octahedral factor μ, which is the radius ratio of B-site cations (r_B) to the X-site anions (r_X) (i.e. $\mu = r_B / r_X$).[62] Both the factors define the formation of potentially stable compounds within A$_2$BX$_6$ family.[63] For mixed Sn-Te perovskite Rb$_2$Sn$_{1-x}$Te$_x$I$_6$, we considered Sn(IV) and Te(IV) as one cation and considered the following expression to calculate the average ionic radii with nearly identical size $r_B = [(1 - x) \times r_{Sn} + x \times r_{Te}]$. For halide perovskite, the empirical stability region is conventionally considered within $0.8 \leq t \leq 1$ and $\mu > 0.414$.[64] If $t < 0.8$, this indicates A-cation is too small for the voids, leading to alternative structures, and if $t > 1$, the A-cation is too large and generally precludes perovskite formation.

From the Shannon ionic radii,[65] we use r_{Rb}=1.72 Å for Rb$^+$, r_{Sn}= 0.69 Å for Sn^{4+}, r_{Te}= 0.97 Å for Te^{4+}, and r_I= 2.20 Å for iodine to get a precise tolerance factor. The calculated t and μ values for a range of Sn-Te composition are summarized in Figure 2 and Table S2. It can be seen that all the structures cover the range where the perovskite phase is stable $0.8 \leq t \leq 1$ and consequently gives evidence that mixed Sn−Te perovskites Rb$_2$Sn$_{1-x}$Te$_x$I$_6$ can be created.
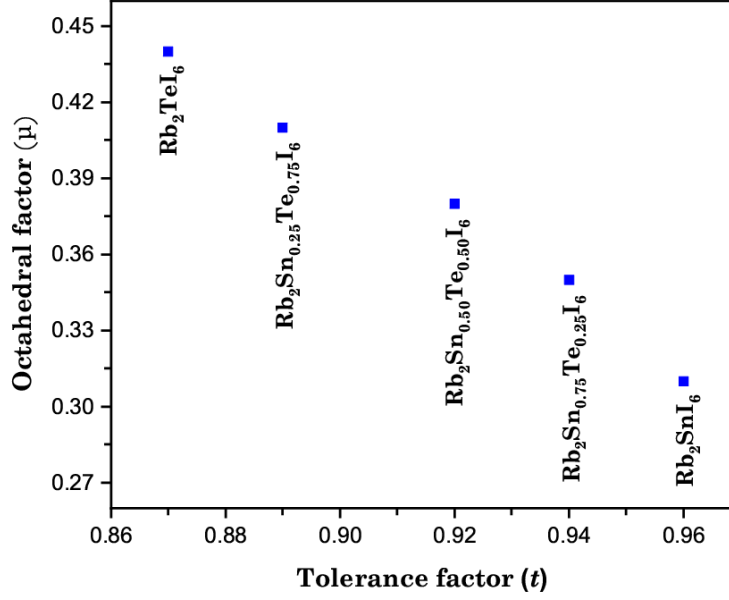
Figure 2. Calculated tolerance and octahedral factors of $Rb_2Sn_{1-x}Te_xI_6$ ($0 \leq x \leq 1$) series.

A bottleneck for commercialization of perovskite-based photovoltaics is their long-term stability. Therefore, we have estimated the formation energies of the parent as well as the mixed perovskites in terms of the possible pathways. According to an earlier report,[41] the formation process of A_2BX_6 perovskite can be defined as follows:

$$A_2BX_6 \rightarrow 2AX + BX_4$$
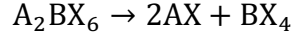
In order to find the stability, we define the formation energy of A_2BX_6 (A= Rb; B= Sn, Te; and X= I) perovskite by the following equation

$$E_f = E(A_2BX_6) - E(2AX) - E(BX_4) \tag{1}$$

where the term E_f represents formation energy, and $E(A_2BX_6)$, $E(2AX)$, and $E(BX_4)$ are the total energies of the compounds involved in the decomposition reaction obtained through PBE method. For Te-doped system, the formation energies are calculated by the following decomposing reaction:

$$E_f = E(Rb_2Sn_{1-x}Te_xI_6) - [E(RbI) + (1-x)E(SnI_4) + xE(I_2) + xE(Te)] \tag{2}$$

where x represents the ratios of 1/4, 1/2, and 3/4. In literature on perovskites, the sign and magnitude of E_f is mostly used to assess the stability of a compound.[42] According to this, a negative E_f means stable geometry i.e. the material is stable whereas positive value represents instability. Moreover, the more negative is E_f, higher will be the stability of the corresponding structure. The obtained results are plotted in Figure 3 which clearly depicts that all the structures exhibit high stability with high negative E_f values. Thus, confirming the formation of stable halide perovskites. Particularly, $Rb_2Sn_{0.75}Te_{0.25}I_6$ and Rb_2TeI_6 perovskites are more stable among $Rb_2Sn_{1-x}Te_xI_6$ based on their calculated formation energy.
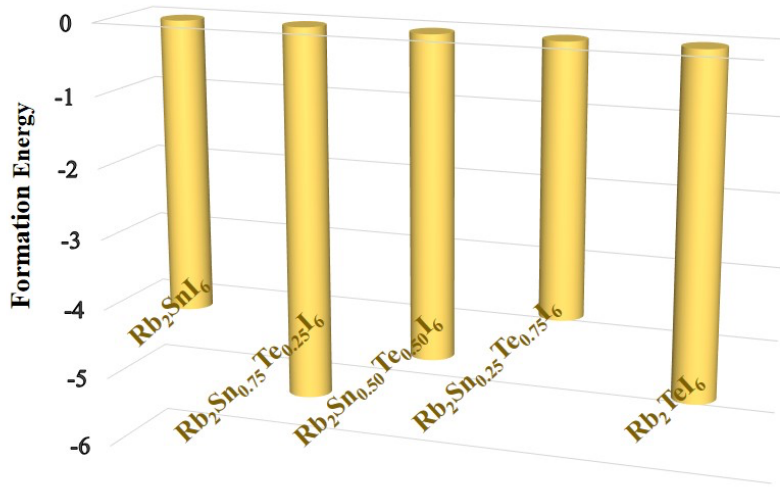

Figure 3. Calculated formation energies (eV) of Sn−Te perovskites with change in Te proportion (0 to 100%).

3.2. Electronic Properties

A key factor for assessing the performance of a solar cell is the electronic band gap of the absorbing material and its transition nature. In order to achieve a theoretical efficiency of > 25%, the band gap value should be within the range of 0.9–1.6 eV.[66] The electronic properties of $Rb_2Sn_{1-x}Te_xI_6$ ($0 \leq x \leq 1$) perovskites are computed using the optimized data listed in Table 1. The band gap calculated using PBE lies in the range of 0.13–1.78 eV (see Table S3). However, it is well known that PBE-GGA severely underestimates the band gap. Therefore, we have performed expensive mBJ and HSE06 calculations for accurate prediction of the band gap. Details of the band gap for $Rb_2Sn_{1-x}Te_xI_6$ ($0 \leq x \leq 1$) alloys with mBJ and HSE06 methods are presented in Figure 4 (corresponding

data is listed in Table S3). Our calculations (in case of both mBJ and HSE06) show an increase in the band gap value with increasing proportion of Te. As shown in Figure 4, the band gap is found to be 0.86 eV, 1.35 eV, 1.44 eV, 1.67 eV and 2.18 eV for $x = 0$, 0.25, 0.50, 0.27, and 1, respectively. It is clear that the change in the band gap is due to the replacement of Sn by Te. As the B-I (B= Sn/Te) bond length increases with Te content, there is an obvious decrease in the interaction between B and I atoms causing less orbital overlap and band dispersions, which leads to the increase in the band gap. The results suggest that two of the compounds, namely $Rb_2Sn_{0.75}Te_{0.25}I_6$ (1.35 eV) and $Rb_2Sn_{0.50}Te_{0.50}I_6$ (1.44 eV) ought to fall within the optimal range and are ideal for single-junction solar cells whereas Rb_2SnI_6 (0.86 eV) and $Rb_2Sn_{0.25}Te_{0.75}I_6$ (1.67 eV), are suitable for tandem solar cell due to their proper band gaps. Meanwhile, Rb_2TeI_6 (2.18 eV) is not suitable for photovoltaic application due to its larger band gap. On the basis of HSE06 calculations, $Rb_2Sn_{0.75}Te_{0.25}I_6$ stands out as the ideal candidate for light harvesting layer due to the optimum band gap. The orbital projected band structures for the representative end members are shown in Figure 5 whereas for the doped systems the band structures plot are presented in the Supporting Information (Figure S2). The orbital projections show that the top of the valence band is dominated by I-$5p$ orbitals, whereas the conduction band minimum (CBM) is derived from hybridization between Sn-5s/or Te-5p and I-5p states. It is well known that a semiconducting material with direct transition nature is more favorable than the indirect nature. Fortunately, among the five compounds, Rb_2SnI_6, $Rb_2Sn_{0.75}Te_{0.25}I_6$, and $Rb_2Sn_{0.50}Te_{0.50}I_6$, are predicted to possess direct band gap nature (at Γ point) while the other two combinations, viz. $Rb_2Sn_{0.25}Te_{0.75}I_6$, and Rb_2TeI_6 exhibit indirect band gap character (Figure 5 and Figure S2). The direct band gap character of Rb_2SnI_6 is consistent with previous results, obtained theoretically.[42] With further exploring the band profile of these perovskites we notice that the transition nature changes with the increase of Te concentration.
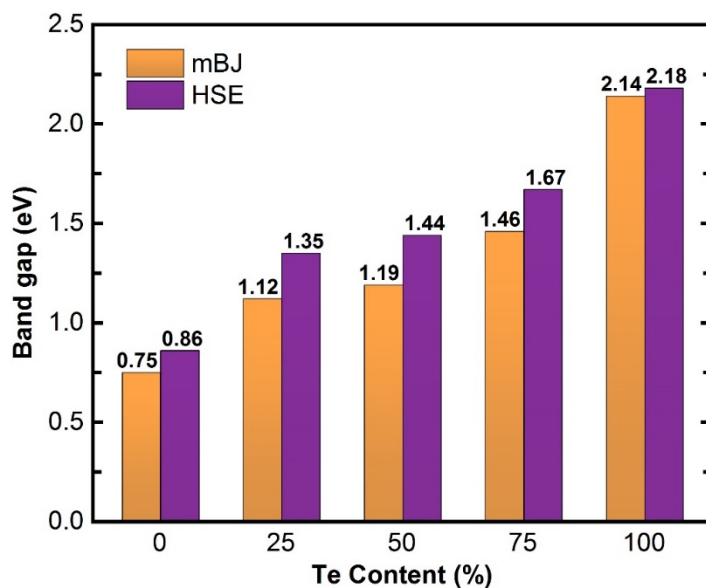
Figure 4. Variation of the band gap by changing the Te contents in $Rb_2Sn_{1-x}Te_xI_6$ ($0 \leq x \leq 1$) perovskites.
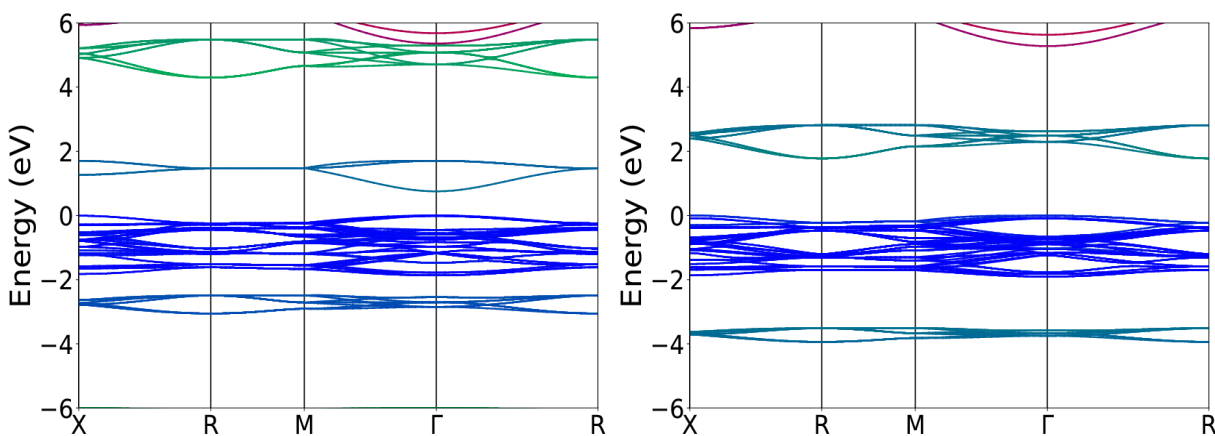

Figure 5. Orbital projected band structure of Rb_2SnI_6 (left) and Rb_2TeI_6 (right) using HSE06 functional. The orbital contribution is represented with Rb $3d$ (red), Sn $5s$ (green), I $5p$ (orange), and Te $5p$ (magenta). The resulting color in the diagram is obtained by mixing each color in accordance with the orbital contributions.

To further understand the nature of valence and conduction bands, the density of states (DOS) are simulated. The projected DOS for the parent as well as the Sn-Te mixed perovskite with HSE06 calculations exhibit similar curves (Figure 6 and Figure S3). The Rb-cation does not contribute to the band edges because the orbitals of Rb are too far from the Fermi level, i.e. the molecules do not take part in the active region. The Rb cation acts as a charge compensator and balance the

charge neutrality of the ionic perovskite system. Thus, for the sake of simplicity around the Fermi level, only the valence orbitals contributions of Sn, Te, and I are presented. The main contribution to the valence band (VB) of all these perovskites is derived predominantly from $5p$ orbitals of halogen anion. While the conduction band (CB) is formed due to the overlap of the B-site ($5s$ for Sn and $5p$ for Te) and I-$5p$ orbitals. For Te doped system, a closer look at the DOS reveals that the states just below the valence band maxima around at an energy of -0.25 eV (responsible for carrier as well as energy transport) contain a mixture of Te-s and halogens p orbitals. Moreover, the calculated DOS is found in close agreement with Cs based A_2BX_6 perovskites.[22, 42] Upon increasing the Te-contributions, we notice that the major contributing orbitals to CB change from Sn-$5s$ to Te-$5p$ i.e. the Sn contribution drops and the contribution of Te increases, as depicted in Figure 6 and Figure S3. This clearly accounts for the increase of the electronic band gap with the Te content in $Rb_2Sn_{1-x}Te_xI_6$ perovskites. Briefly, we can say that the solar energy conversion properties, which were primarily controlled by Sn^{4+} in Rb_2SnI_6 are now controlled by the new hybrid orbitals of Te^{4+} and Sn^{4+} in the mixed $Rb_2Sn_{1-x}Te_xI_6$ perovskite.
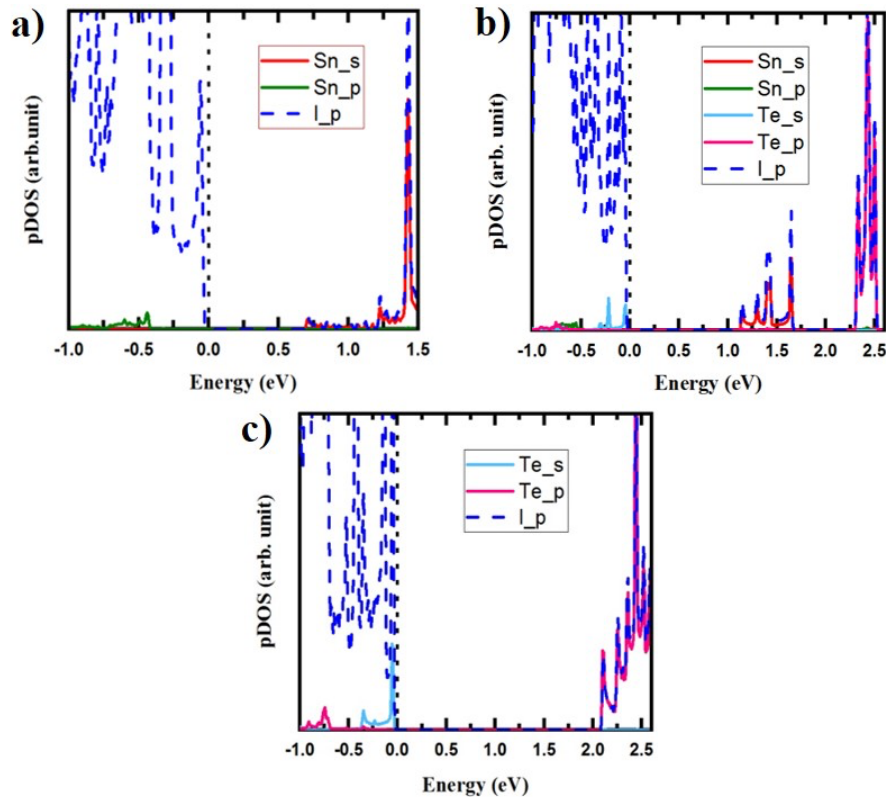

Figure 6. Projected density of states (pDOS) of (a) 0% Te (Rb_2SnI_6), (b) 50% Te ($Rb_2Sn_{0.50}Te_{0.50}I_6$), and (c) 100% Te ($Rb_2TeI_6$).

3.3. Optical Properties

Optical properties such as large dielectric constant and strong optical absorption are very crucial for high performance of solar cells. In optical properties, we evaluated the dielectric constants, absorption coefficients, effective masses, exciton binding energy, and spectroscopic limited maximum efficiency (SLME), keeping in mind the requisites of solar cells applications. The complex dielectric function, $\varepsilon(\omega) = \varepsilon_1(\omega) + \varepsilon_2(\omega)$, describes the optical response of a material to incident light energy and is calculated on the basis of linear response method.[67-68] The real part of the dielectric function shows electronic polarizability of a material whereas the imaginary part gives information about the absorption behavior of a crystal. The charge-carrier recombination rate and the complete behavior of semiconducting optoelectronic devices is mainly determined by the static value of $\varepsilon(\omega)$. Any material with a large dielectric constant possesses relatively less charge-carrier recombination rate resulting in improved performance of an optoelectronic device. The dielectric spectra of the corresponding $Rb_2Sn_{1-x}Te_xI_6$ ($0 \leq x \leq 1$) perovskites are calculated as functions of photon energy from zero to 5 eV. The real part of $\varepsilon(\omega)$ of pure and doped Rb_2SnI_6 are shown in Figure 7 and Figure S4. The static spectral components, $\varepsilon_0(\omega)$ are found to be 4.20, 4.32, 5.14, 5.22, and 5.27, for x = 0.0, 0.25, 0.50, 0.75, and 1, respectively. The results clearly reveal anisotropy in the optical properties of cubic $Rb_2Sn_{1-x}Te_xI_6$. The increase in the value of $\varepsilon_0(\omega)$ with increasing Te-proportion may indicate a smaller exciton binding energy. Beyond the zero frequency limit, $\varepsilon_1(\omega)$ starts to increase with the increase of photon energy, reaching the maximum at certain photon energies (See Figure 7 and Table 2). Among the five real parts, the amplitude of the peaks becomes larger in the case of $Rb_2Sn_{0.50}Te_{0.50}I_6$ with a maximum peak value of 11.77 at 2.30 eV (see Figure 7c). The spectra of $Rb_2Sn_{0.75}Te_{0.25}I_6$ contain three main peaks at 1.05 eV, 2.25 eV, and 3.57 eV, followed by a small peak in the ultraviolet region (4.72 eV). It is obvious that the Te-doped systems show somewhat high dielectric constant than the pure Rb_2SnI_6. Further, it should be noted that for all the systems, most of the major peaks are centered in the energy range ~1.1−3.7 eV. However, with the increase of Te contents, the curves are redshifted towards the visible region, causing an increase in $\varepsilon_1(\omega)$ spectra and shifting the peaks towards smaller photon energies.

A similar trend has also been observed for the imaginary part of the dielectric function, shown in Figure 7 and Figure S4. For Rb_2SnI_6 as well as for Te-doped (x = 0.25 and 0.50) systems, the spectra contain three main peaks (labelled as I, II, and III) with multiple shoulders at different

energy zones. Initially, the value of $\varepsilon_2(\omega)$ starts to increase at photon energies equal or greater than the fundamental band gap. With the increase of the Te-proportion, the magnitude of $\varepsilon_2(\omega)$ becomes larger and the peaks on the curve get more pronounced in the visible range of the spectrum. As the $\varepsilon_2(\omega)$ spectra correspond closely to the DOS, so the peaks can be attributed to the orbitals transitions between VB and CB. In particular, the low energy peaks are mainly associated with the transition between I-$5p$ orbitals in the uppermost valence band to Sn-$5s$/Te-$5p$ orbitals in the conduction band. For $Rb_2Sn_{0.50}Te_{0.50}I_6$, a strongest peak is observed at about 1.50 eV, indicating strong absorption in this region compared with other systems. Also, for $Rb_2Sn_{0.25}Te_{0.75}I_6$ and Rb_2TeI_6, no extra features have been observed except a broad peak at ~2.90 eV. We conclude that in terms of the dielectric constant, $Rb_2Sn_{0.50}Te_{0.50}I_6$ is a suitable choice for optoelectronics and solar cell applications.

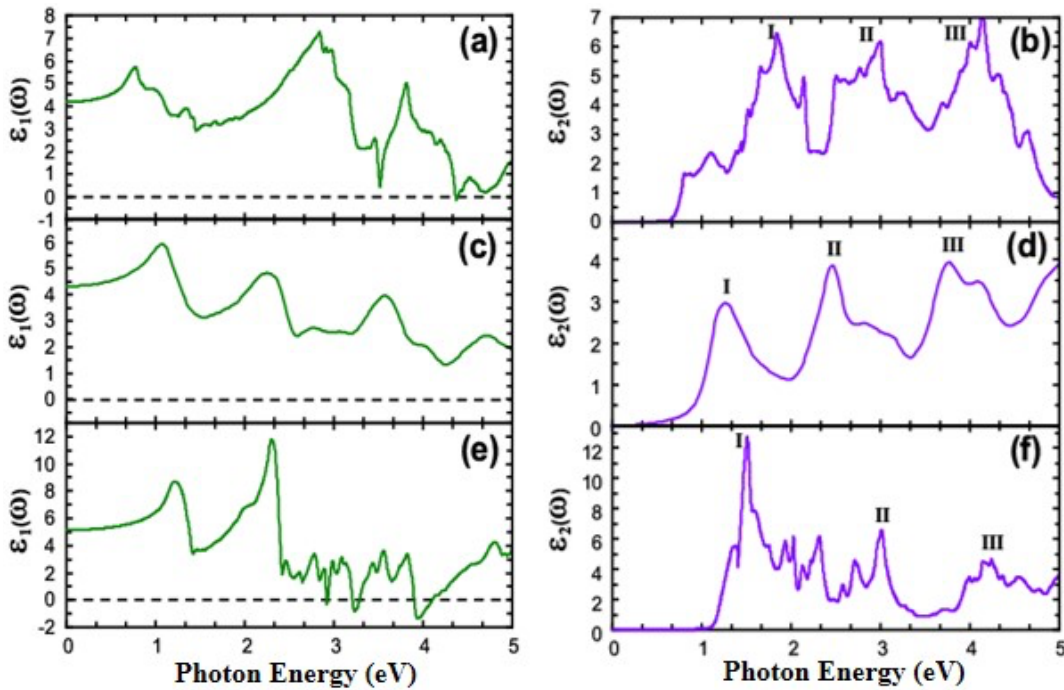**Figure 7.** Calculated real $\varepsilon_1(\omega)$ and imaginary $\varepsilon_2(\omega)$ parts of the dielectric function of $Rb_2Sn_{1-x}Te_xI_6$ ($x = 0.0, 0.25, 0.50$) perovskites.

Carrier transport is another essential property for efficient solar cell absorbers. The effective masses of electron and holes contribute significantly to the mobility of the carrier inside the solar cell. To assess the carrier mobility, the carrier effective masses of $Rb_2Sn_{1-x}Te_xI_6$ are calculated

around the band edges according to $m^* = \hbar^2 \left[\frac{\partial^2 \varepsilon(k)}{\partial^2 k}\right]^{-1}$, $\varepsilon(k)$ is the band edge eigenvalue and k is the wave vector. Since both the electrons and holes in $Rb_2Sn_{1-x}Te_xI_6$ thermally relax to the bottom of the CB and top of the VB consequently, their effective masses (listed in Table 2) are calculated from the HSE06 band structure according to the above expression. The reduced effective mass has also been calculated using $\mu = m_e.m_h/(m_e + m_h)$. In general, the more dispersive is the band near the edges, the smaller will be the effective mass and vice versa. Altogether, the holes are found heavier than the electron, which indicates good electron transport. This may be due to the fact that the lowest conduction band, derived primarily from more delocalized Sn-s/Te-p orbitals, is more dispersive than the highest valence band, derived predominantly from low energy halogens p orbitals. Therefore, the electron effective mass is smaller than the hole. From Table 2, relatively small m_e^* values are found for the end-members as well as for the mixed Sn-Te perovskite (with $x = 0.75$), suggesting their better carrier transport ability important for better PCE of a solar cell. In contrast the hole mass m_h^* spans over the range $1.28-1.77m_0$ (m_0 is the electron static mass). It is worth noting that in all the perovskites under investigation in our project, the variations of effective mass is more complex due to the presence of multiple valence bands around the band edge. To account for the excitonic effect, the exciton binding energies were calculated and listed in Table 2. The exciton binding energies were estimated using the dielectric constant and reduced effective mass. We calculated two types of the exciton binding energy, E_b, calculated on the basis of static dielectric constant by including the phonon contributions and , $\tilde{E}_b$, calculated using maximum dielectric constant without taking into account phonon contributions. We observed that the dielectric constant and the exciton binding energy vary in inverse.

Table 2. The static and maximum dielectric constant (ε_0 and ε_∞), calculated effective masses of electron, holes, and its reduced mass, exciton binding energies (meV) calculate using the static and maximum dielectric constant for $Rb_2Sn_{1-x}Te_xI_6$ Perovskites (Using HSE06 Functional).

	Dielectric constant		Effective masses (m_e)			Exciton binding energy	
	$\varepsilon_0(\omega)$	$\varepsilon_\infty(\omega)$	m_e^*	m_h^*	μ	E_b	$\tilde{E}_b$
0% Te (Rb_2SnI_6)	4.20	7.27	0.15	1.28	0.13	100.40	33.43
25% Te ($Rb_2Sn_{0.75}Te_{0.25}I_6$)	4.32	6.01	0.39	1.77	0.32	233.09	120.09
50% Te ($Rb_2Sn_{0.50}Te_{0.50}I_6$)	5.14	11.78	0.42	1.60	0.33	169.76	32.34

75% Te ($Rb_2Sn_{0.25}Te_{0.75}I_6$)	5.23	10.18	0.31	1.63	0.26	129.37	34.10
100% Te (Rb_2TeI_6)	5.27	9.55	0.23	1.54	0.20	97.84	29.80

 A very important parameter in photovoltaics characterization, the absorption coefficient, of these compounds was calculated in the visible range as presented in Figure 8, as a function of photon energy. A significant variation can be seen in the profile of different curves, suggesting a gradual increase of the absorption onset with increasing Te content. The absorption coefficient of Rb_2SnI_6 seems to be largely influenced by the presence of the Te dopant. For all these perovskites, high absorption ($\sim10^5$ cm^{-1}) is found in the visible part of the spectrum and multiple peak character can be seen with valleys between the peaks. Among the investigated series, the strongest absorption, about 6.9×10^5 cm^{-1}, occurs approximately at 1.97 eV for $Rb_2Sn_{0.75}Te_{0.25}I_6$. Similarly, for $Rb_2Sn_{0.50}Te_{0.50}I_6$, a maximum absorption strength of 6.04×10^5 cm^{-1} can be found at 2.6 eV. Both the compounds possess a broad absorption spectrum in the visible range (1.50–2.60 eV), showing a great promise for use as absorbing layers in PSCs. Further, we notice that the absorption strength is significantly high in the mixed Sn-Te perovskite as compared to the end-members.

In the Shockley–Queisser scheme[66], solar cell efficiency mainly depends on the band gap value, which is regarded as a primary metric for efficient PV materials. However, band gap is not the only factor to evaluate the performance of a solar cell. In fact, strong visible light absorption, the allowed band gap nature (direct/indirect), and the thickness of a solar absorber layer are also crucial for achieving highly efficient PSCs. Taking the above factors into account, the spectroscopic-limited-maximum-efficiency (SLME) metric is calculated according to the method adopted by Yu and Zunger.[69] The SLME method has shown superiority over the Shockley–Queisser limit in several ways; (i) the non-radiative recombination rate is approximated, which is based on the difference between the fundamental band gap and the lowest allowed optical transition, (ii) the optical absorption depending on frequency (ω) taken into account, and (iii) the thickness of the absorber layer is also considered. Using the above screening criteria, the SLME for the compounds under investigation is evaluated and presented in Figure 8. The predicted compounds have shown to possess large SLME in our calculation. The compound, namely $Rb_2Sn_{0.50}Te_{0.50}I_6$, exhibit the highest efficiency correlated with its favorable band gap and high optical absorption.
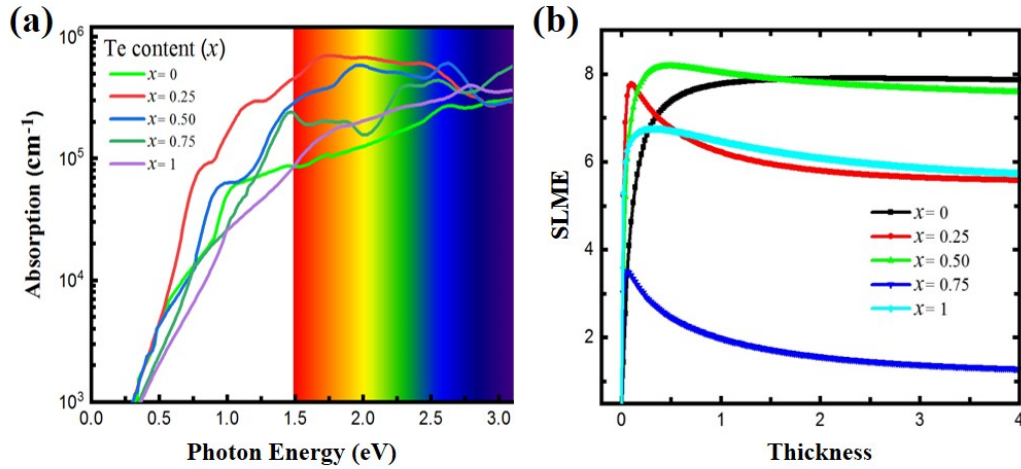
Figure 8. (a) Calculated absorption spectra of the Te-doped A_2BX_6 perovskites. (b) SLME of $Rb_2Sn_{1-x}Te_xI_6$ perovskite with respect to the film thickness.

4. Conclusions

We computed the crystal structure, formation energies, electronic, and optical properties of defect variant perovskite $Rb_2Sn_{1-x}Te_xI_6$ ($0 \leq x \leq 1$) using first-principles method based on the density functional theory. The alloying of the B-site Sn and Te has been explored in detailed for tuning the band gap and structural stability of A_2BX_6 compounds. We mainly focus on the structural stability, electronic band gap, static and maximum dielectric constants, absorption spectra, and effective masses of the considered systems using PBE-GGA, mBJ, and HSE06 functionals. The calculated structural parameters obtained at PBE-level have been found in good agreement with the available experiments. The results show an increasing trend in the band gap with the increasing Te proportion across the compounds. These perovskites possess band gap in the range 0.86 eV to 2.18 eV, making them suitable materials for a wide variety of optoelectronic applications including single and multi-junction PSCs. The orbital projected band structure and density of states show that the top of the valence band is mainly contributed by I-$5p$ orbitals, whereas bottom of the conduction band is derived from mixed Sn-$5s$/or Te-$5p$ and I-$5p$ orbitals. Optical properties analyses indicate that mixed halide perovskites appear superior to pure Sn and/ or Te counterparts, as the former possess strong optical absorption and high photoelectric conversion efficiency than the pristine compounds. This study reveals that the band gap as well as the optical absorption strongly depend upon the quantity of Sn replaced with Te. Further, all these perovskites possess

moderate effective masses indicating their optimum carrier transport properties. The overall analysis of structural stability, electronic, and optical properties suggest that the compounds $Rb_2Sn_{0.75}Te_{0.25}I_6$ and $Rb_2Sn_{0.50}Te_{0.50}I_6$ become the potential candidates for applications such as solar photoabsorbers. You may also include a few words about their chances of being synthesized in a lab.

Acknowledgments

References

1.   Burschka, J.; Pellet, N.; Moon, S.-J.; Humphry-Baker, R.; Gao, P.; Nazeeruddin, M. K.; Grätzel, M., Sequential deposition as a route to high-performance perovskite-sensitized solar cells. *Nature* **2013,** *499* (7458), 316.

2.   Stranks, S. D.; Eperon, G. E.; Grancini, G.; Menelaou, C.; Alcocer, M. J.; Leijtens, T.; Herz, L. M.; Petrozza, A.; Snaith, H. J., Electron-hole diffusion lengths exceeding 1 micrometer in an organometal trihalide perovskite absorber. *Science* **2013,** *342* (6156), 341-344.

3.   Jung, H. S.; Park, N. G., Perovskite solar cells: from materials to devices. *small* **2015,** *11* (1), 10-25.

4.   Antoniadou, M.; Siranidi, E.; Vaenas, N.; Kontos, A.; Stathatos, E.; Falaras, P., Photovoltaic Performance and Stability of CH3NH3PbI3–x Cl x Perovskites. *Journal of Surfaces and Interfaces of Materials* **2014,** *2* (4), 323-327.

5.   NREL, Best Research-Cell Efficiencies (NREL, 2019) https://www.nrel.gov/pv/assets/pdfs/best-research-cell-efficiencies.20190802.pdf. **2019**.

6.   Bailie, C. D.; Christoforo, M. G.; Mailoa, J. P.; Bowring, A. R.; Unger, E. L.; Nguyen, W. H.; Burschka, J.; Pellet, N.; Lee, J. Z.; Grätzel, M., Semi-transparent perovskite solar cells for tandems with silicon and CIGS. *Energy & Environmental Science* **2015,** *8* (3), 956-963.

7.   Chen, H.; Xiang, S.; Li, W.; Liu, H.; Zhu, L.; Yang, S., Inorganic Perovskite Solar Cells: A Rapidly Growing Field. *Solar RRL* **2018,** *2* (2), 1700188.

8.   Sun, S.; Salim, T.; Mathews, N.; Duchamp, M.; Boothroyd, C.; Xing, G.; Sum, T. C.; Lam, Y. M., The origin of high efficiency in low-temperature solution-processable bilayer organometal halide hybrid solar cells. *Energy & Environmental Science* **2014,** *7* (1), 399-407.

9.   Li, F.; Ma, C.; Wang, H.; Hu, W.; Yu, W.; Sheikh, A. D.; Wu, T., Ambipolar solution-processed hybrid perovskite phototransistors. *Nature communications* **2015,** *6*, 8238.

10.   Hailegnaw, B.; Kirmayer, S.; Edri, E.; Hodes, G.; Cahen, D., Rain on methylammonium lead iodide based perovskites: possible environmental effects of perovskite solar cells. *The journal of physical chemistry letters* **2015,** *6* (9), 1543-1547.

11.   Song, Z.; Abate, A.; Watthage, S. C.; Liyanage, G. K.; Phillips, A. B.; Steiner, U.; Graetzel, M.; Heben, M. J., Perovskite Solar Cell Stability in Humid Air: Partially Reversible Phase Transitions in the PbI2-CH3NH3I-H2O System. *Advanced Energy Materials* **2016,** *6* (19), 1600846.

12.   Tan, Z.; Li, J.; Zhang, C.; Li, Z.; Hu, Q.; Xiao, Z.; Kamiya, T.; Hosono, H.; Niu, G.; Lifshitz, E., Highly Efficient Blue-Emitting Bi-Doped Cs2SnCl6 Perovskite Variant: Photoluminescence Induced by Impurity Doping. *Advanced Functional Materials* **2018,** *28* (29), 1801131.

13.   Ju, M.-G.; Chen, M.; Zhou, Y.; Garces, H. F.; Dai, J.; Ma, L.; Padture, N. P.; Zeng, X. C., Earth-abundant nontoxic titanium (IV)-based vacancy-ordered double perovskite halides with tunable 1.0 to 1.8 eV bandgaps for photovoltaic applications. *ACS Energy Letters* **2018,** *3* (2), 297-304.

14.   Swarnkar, A.; Ravi, V. K.; Nag, A., Beyond colloidal cesium lead halide perovskite nanocrystals: analogous metal halides and doping. *ACS Energy Letters* **2017,** *2* (5), 1089-1098.

15.   Yang, B.; Li, Y.-J.; Tang, Y.-X.; Mao, X.; Luo, C.; Wang, M.-S.; Deng, W.-Q.; Han, K.-L., Constructing sensitive and fast lead-free single-crystalline perovskite photodetectors. *The journal of physical chemistry letters* **2018,** *9* (11), 3087-3092.

16.   Lee, M. M.; Teuscher, J.; Miyasaka, T.; Murakami, T. N.; Snaith, H. J., Efficient hybrid solar cells based on meso-superstructured organometal halide perovskites. *Science* **2012**, 1228604.

17.   Hao, F.; Stoumpos, C. C.; Cao, D. H.; Chang, R. P.; Kanatzidis, M. G., Lead-free solid-state organic–inorganic halide perovskite solar cells. *Nature Photonics* **2014,** *8* (6), 489.

18.   Noel, N. K.; Stranks, S. D.; Abate, A.; Wehrenfennig, C.; Guarnera, S.; Haghighirad, A.-A.; Sadhanala, A.; Eperon, G. E.; Pathak, S. K.; Johnston, M. B., Lead-free organic–inorganic tin halide perovskites for photovoltaic applications. *Energy & Environmental Science* **2014,** *7* (9), 3061-3068.

19.   Lee, B.; Ezhumalai, Y.; Lee, W.; Chen, M.-C.; Yeh, C.-Y.; Marks, T. J.; Chang, R. P., Cs2SnI6-Encapsulated Multidye-Sensitized All-Solid-State Solar Cells. *ACS applied materials & interfaces* **2019,** *11* (24), 21424-21434.

20.   Liao, W.; Zhao, D.; Yu, Y.; Grice, C. R.; Wang, C.; Cimaroli, A. J.; Schulz, P.; Meng, W.; Zhu, K.; Xiong, R. G., Lead-free inverted planar formamidinium tin triiodide perovskite solar cells achieving power conversion efficiencies up to 6.22%. *Advanced materials* **2016,** *28* (42), 9333-9340.

21.   Park, B. W.; Philippe, B.; Zhang, X.; Rensmo, H.; Boschloo, G.; Johansson, E. M., Bismuth based hybrid perovskites A3Bi2I9 (A: methylammonium or cesium) for solar cell application. *Advanced materials* **2015,** *27* (43), 6806-6813.

22.   Maughan, A. E.; Ganose, A. M.; Bordelon, M. M.; Miller, E. M.; Scanlon, D. O.; Neilson, J. R., Defect tolerance to intolerance in the vacancy-ordered double perovskite semiconductors Cs2SnI6 and Cs2TeI6. *Journal of the American Chemical Society* **2016,** *138* (27), 8453-8464.

23.   Saparov, B.; Sun, J.-P.; Meng, W.; Xiao, Z.; Duan, H.-S.; Gunawan, O.; Shin, D.; Hill, I. G.; Yan, Y.; Mitzi, D. B., Thin-film deposition and characterization of a Sn-deficient perovskite derivative Cs2SnI6. *Chemistry of Materials* **2016,** *28* (7), 2315-2322.

24.   Giustino, F.; Snaith, H. J., Toward lead-free perovskite solar cells. *ACS Energy Letters* **2016,** *1* (6), 1233-1240.

25.   Zhang, Q.; Ting, H.; Wei, S.; Huang, D.; Wu, C.; Sun, W.; Qu, B.; Wang, S.; Chen, Z.; Xiao, L., Recent progress in lead-free perovskite (-like) solar cells. *Materials today energy* **2018,** *8*, 157-165.

26.   Meng, W.; Wang, X.; Xiao, Z.; Wang, J.; Mitzi, D. B.; Yan, Y., Parity-forbidden transitions and their impact on the optical absorption properties of lead-free metal halide perovskites and double perovskites. *The journal of physical chemistry letters* **2017,** *8* (13), 2999-3007.

27.   Saparov, B.; Hong, F.; Sun, J.-P.; Duan, H.-S.; Meng, W.; Cameron, S.; Hill, I. G.; Yan, Y.; Mitzi, D. B., Thin-film preparation and characterization of Cs3Sb2I9: A lead-free layered perovskite semiconductor. *Chemistry of Materials* **2015,** *27* (16), 5622-5632.

28.   Du, K. z.; Meng, W.; Wang, X.; Yan, Y.; Mitzi, D. B., Bandgap Engineering of Lead-Free Double Perovskite Cs2AgBiBr6 through Trivalent Metal Alloying. *Angewandte Chemie International Edition* **2017,** *56* (28), 8158-8162.

29.   Chen, M.; Ju, M.-G.; Carl, A. D.; Zong, Y.; Grimm, R. L.; Gu, J.; Zeng, X. C.; Zhou, Y.; Padture, N. P., Cesium titanium (IV) bromide thin films based stable lead-free perovskite solar cells. *Joule* **2018,** *2* (3), 558-570.

30.   Lee, B.; Stoumpos, C. C.; Zhou, N.; Hao, F.; Malliakas, C.; Yeh, C.-Y.; Marks, T. J.; Kanatzidis, M. G.; Chang, R. P., Air-stable molecular semiconducting iodosalts for solar cell applications: Cs2SnI6 as a hole conductor. *Journal of the American Chemical Society* **2014,** *136* (43), 15379-15385.

31.   Kaltzoglou, A.; Antoniadou, M.; Kontos, A. G.; Stoumpos, C. C.; Perganti, D.; Siranidi, E.; Raptis, V.; Trohidou, K.; Psycharis, V.; Kanatzidis, M. G., Optical-vibrational properties of the Cs2SnX6 (X= Cl, Br, I) defect perovskites and hole-transport efficiency in dye-sensitized solar cells. *The Journal of Physical Chemistry C* **2016,** *120* (22), 11777-11785.

32.   Karim, M. M.; Ganose, A. M.; Pieters, L.; Winnie Leung, W.; Wade, J.; Zhang, L.; Scanlon, D. O.; Palgrave, R. G., Anion distribution, structural distortion, and symmetry-driven optical band gap bowing in mixed halide Cs2SnX6 vacancy ordered double perovskites. *Chemistry of Materials* **2019,** *31* (22), 9430-9444.

33.   Maughan, A. E.; Ganose, A. M.; Almaker, M. A.; Scanlon, D. O.; Neilson, J. R., Tolerance factor and cooperative tilting effects in vacancy-ordered double perovskite halides. *Chemistry of Materials* **2018,** *30* (11), 3909-3919.

34.   Werker, W., Die Krystallstruktur des Rb2SnJ6 und Cs2SnJ6. *Recueil des Travaux Chimiques des Pays‑Bas* **1939,** *58* (3), 257-258.

35.   Jong, U.-G.; Yu, C.-J.; Kye, Y.-H., Computational prediction of structural, electronic, and optical properties and phase stability of double perovskites K 2 SnX 6 (X= I, Br, Cl). *RSC Advances* **2020,** *10* (1), 201-209.

36.   Kaltzoglou, A.; Antoniadou, M.; Perganti, D.; Siranidi, E.; Raptis, V.; Trohidou, K.; Psycharis, V.; Kontos, A. G.; Falaras, P., Mixed-halide Cs2SnI3Br3 perovskite as low resistance hole-transporting material in dye-sensitized solar cells. *Electrochimica Acta* **2015,** *184*, 466-474.

37.   Bounos, G.; Karnachoriti, M.; Kontos, A. G.; Stoumpos, C. C.; Tsetseris, L.; Kaltzoglou, A.; Guo, X.; Lü, X.; Raptis, Y. S.; Kanatzidis, M. G., Defect Perovskites under Pressure: Structural Evolution of Cs2SnX6 (X= Cl, Br, I). *The Journal of Physical Chemistry C* **2018,** *122* (42), 24004-24013.

38.   Ma, X. X.; Li, Z. S., Influence of Sn/Ge Cation Exchange on Vacancy-Ordered Double Perovskite Cs2Sn (1− x) GexI6: A First-Principles Theoretical Study. *physica status solidi (b)* **2019,** *256* (3), 1800427.

39.   Sakai, N.; Haghighirad, A. A.; Filip, M. R.; Nayak, P. K.; Nayak, S.; Ramadan, A.; Wang, Z.; Giustino, F.; Snaith, H. J., Solution-processed cesium hexabromopalladate (IV), Cs2PdBr6, for optoelectronic applications. *Journal of the American Chemical Society* **2017,** *139* (17), 6030-6033.

40.   Zhou, L.; Liao, J.-F.; Huang, Z.-G.; Wang, X.-D.; Xu, Y.-F.; Chen, H.-Y.; Kuang, D.-B.; Su, C.-Y., All-inorganic lead-free Cs2PdX6 (X= Br, I) perovskite nanocrystals with single unit cell thickness and high stability. *ACS Energy Letters* **2018,** *3* (10), 2613-2619.

41.   Schwartz, D., Cesium Platinum Iodide Perovskite Synthesis, Development and Application in Photovoltaic Devices. **2019**.

42.   Cai, Y.; Xie, W.; Ding, H.; Chen, Y.; Thirumal, K.; Wong, L. H.; Mathews, N.; Mhaisalkar, S. G.; Sherburne, M.; Asta, M., Computational Study of Halide Perovskite-Derived A2BX6 Inorganic Compounds: Chemical Trends in Electronic Structure and Structural Stability. *Chemistry of Materials* **2017,** *29* (18), 7740-7749.

43.   Faizan, M.; Bhamu, K.; Khan, S.; Murtaza, G.; He, X., Effect of Cations Transmutation on the Electronic Structure and Optical Properties of Lead-Free Perovskites A2BX6. *arXiv preprint arXiv:2002.07543* **2020**.

44.   Bhamu, K.; Soni, A.; Sahariya, J., Revealing optoelectronic and transport properties of potential perovskites Cs2PdX6 (X= Cl, Br): A probe from density functional theory (DFT). *Solar Energy* **2018,** *162*, 336-343.

45.   Niu, G.; Yu, H.; Li, J.; Wang, D.; Wang, L., Controlled orientation of perovskite films through mixed cations toward high performance perovskite solar cells. *Nano Energy* **2016,** *27*, 87-94.

46.   Zhou, Y.; Chen, J.; Bakr, O. M.; Sun, H.-T., Metal-doped lead halide perovskites: synthesis, properties, and optoelectronic applications. *Chemistry of Materials* **2018,** *30* (19), 6589-6613.

47.   Tang, G.; Hong, J., Direct tuning of the band gap via electronically-active organic cations and large piezoelectric response in one-dimensional hybrid halides from first-principles. *Journal of Materials Chemistry C* **2018,** *6* (28), 7671-7676.

48.   Tang, G.; Xiao, Z.; Hosono, H.; Kamiya, T.; Fang, D.; Hong, J., Layered Halide Double Perovskites Cs3+ n M (II) n Sb2X9+ 3 n (M= Sn, Ge) for Photovoltaic Applications. *The journal of physical chemistry letters* **2018,** *9* (1), 43-48.

49.   Zhou, Y.; Yong, Z.-J.; Zhang, K.-C.; Liu, B.-M.; Wang, Z.-W.; Hou, J.-S.; Fang, Y.-Z.; Zhou, Y.; Sun, H.-T.; Song, B., Ultrabroad photoluminescence and electroluminescence at new wavelengths from doped organometal halide perovskites. *The journal of physical chemistry letters* **2016,** *7* (14), 2735-2741.

50.   Zhao, Z.; Gu, F.; Li, Y.; Sun, W.; Ye, S.; Rao, H.; Liu, Z.; Bian, Z.; Huang, C., Mixed-Organic-Cation Tin Iodide for Lead-Free Perovskite Solar Cells with an Efficiency of 8.12%. *Advanced Science* **2017,** *4* (11), 1700204.

51.   Yuan, G.; Huang, S.; Qin, S.; Wu, X.; Ding, H.; Lu, A., Structural, Optical, and Thermal Properties of Cs2SnI6–xBrx Mixed Perovskite Solid Solutions. *European Journal of Inorganic Chemistry* **2019,** *2019* (20), 2524-2529.

52.   Kresse, G.; Furthmüller, J., Efficient iterative schemes for ab initio total-energy calculations using a plane-wave basis set. *Physical review B* **1996,** *54* (16), 11169.

53.   Kresse, G.; Joubert, D., From ultrasoft pseudopotentials to the projector augmented-wave method. *Physical review b* **1999,** *59* (3), 1758.

54.   Pulay, P., Ab initio calculation of force constants and equilibrium geometries in polyatomic molecules: I. Theory. *Molecular Physics* **1969,** *17* (2), 197-204.

55.   Perdew, J. P.; Burke, K.; Ernzerhof, M., Generalized gradient approximation made simple. *Physical review letters* **1996,** *77* (18), 3865.

56. Tran, F.; Blaha, P., Accurate band gaps of semiconductors and insulators with a semilocal exchange-correlation potential. *Physical review letters* **2009,** *102* (22), 226401.

57. Heyd, J.; Scuseria, G. E.; Ernzerhof, M., Hybrid functionals based on a screened Coulomb potential. *The Journal of chemical physics* **2003,** *118* (18), 8207-8215.

58. Monkhorst, H. J.; Pack, J. D., Special points for Brillouin-zone integrations. *Physical review B* **1976,** *13* (12), 5188.

59. Momma, K.; Izumi, F., VESTA 3 for three-dimensional visualization of crystal, volumetric and morphology data. *Journal of applied crystallography* **2011,** *44* (6), 1272-1276.

60. Abriel, W., Crystal structure and phase transition of Rb2TeI6. *Materials Research Bulletin* **1982,** *17* (10), 1341-1346.

61. Goldschmidt, V. M., Die gesetze der krystallochemie. *Naturwissenschaften* **1926,** *14* (21), 477-485.

62. Li, C.; Soh, K. C. K.; Wu, P., Formability of ABO3 perovskites. *Journal of alloys and compounds* **2004,** *372* (1-2), 40-48.

63. Fedorovskiy, A. E.; Drigo, N. A.; Nazeeruddin, M. K., The Role of Goldschmidt's Tolerance Factor in the Formation of A2BX6 Double Halide Perovskites and its Optimal Range. *Small Methods* **2020,** *4* (5), 1900426.

64. Li, C.; Lu, X.; Ding, W.; Feng, L.; Gao, Y.; Guo, Z., Formability of ABX3 (X= F, Cl, Br, I) Halide Perovskites. *Acta Crystallographica Section B: Structural Science* **2008,** *64* (6), 702-707.

65. Shannon, R. D., Revised effective ionic radii and systematic studies of interatomic distances in halides and chalcogenides. *Acta crystallographica section A: crystal physics, diffraction, theoretical and general crystallography* **1976,** *32* (5), 751-767.

66. Shockley, W.; Queisser, H. J., Detailed balance limit of efficiency of p-n junction solar cells. *Journal of applied physics* **1961,** *32* (3), 510-519.

67. Wooten, F., *Optical properties of solids*. Academic press: 2013.

68. Ambrosch-Draxl, C.; Sofo, J. O., Linear optical properties of solids within the full-potential linearized augmented planewave method. *Computer physics communications* **2006,** *175* (1), 1-14.

69. Yu, L.; Zunger, A., Identification of potential photovoltaic absorbers based on first-principles spectroscopic screening of materials. *Physical review letters* **2012,** *108* (6), 068701.